The Astrophysical Journal, 931:131 (13pp), 2022 June 1 https://doi.org/10.3847/1538-4357/ac67ee

Metallicity of Galactic RR Lyrae from Optical and Infrared Light Curves. II. Period–Fourier–Metallicity Relations for First Overtone RR Lyrae

Joseph P. Mullen[1], Massimo Marengo[1], Clara E. Martínez-Vázquez[2,3], Giuseppe Bono[4,5], Vittorio F. Braga[5,6], Brian Chaboyer[7], Juliana Crestani[4,5,8], Massimo Dall'Ora[9], Michele Fabrizio[5,6], Giuliana Fiorentino[5], Matteo Monelli[10,11], Jillian R. Neeley[12], Peter B. Stetson[13], and Frédéric Thévenin[14]
[1] Department of Physics and Astronomy, Iowa State University, Ames, IA 50011, USA; jpmullen@iastate.edu
[2] Gemini Observatory, NSF's NOIRLaboratory, 670 N. A'ohoku Place, Hilo, HI 96720, USA
[3] Cerro Tololo Inter–American Observatory, NSF's NOIRLaboratory, Casilla 603, La Serena, Chile
[4] Dipartimento di Fisica, Università di Roma Tor Vergata, via della Ricerca Scientifica 1, I-00133 Roma, Italy
[5] INAF—Osservatorio Astronomico di Roma, via Frascati 33, I-00078 Monte Porzio Catone, Italy
[6] Space Science Data Center—ASI, via del Politecnico snc, I-00133 Roma, Italy
[7] Department of Physics and Astronomy, Dartmouth College, 6127 Wilder Laboratory, Hanover, NH 03755, USA
[8] Departamento de Astronomia, Universidade Federal do Rio Grande do Sul, Avenida Bento Gonçalves 6500, Porto Alegre 91501-970, Brazil
[9] INAF—Osservatorio Astronomico di Capodimonte, Salita Moiariello 16, I-80131 Napoli, Italy
[10] IAC- Instituto de Astrofísica de Canarias Calle Vía Lactea s/n, E-38205 La Laguna, Tenerife, Spain
[11] Departmento de Astrofísica, Universidad de La Laguna, E-38206 La Laguna, Tenerife, Spain
[12] Department of Physics, Florida Atlantic University, 777 Glades Road, Boca Raton, FL 33431, USA
[13] Herzberg Astronomy and Astrophysics, National Research Council, 5071 West Saanich Road, Victoria, British Columbia V9E 2E7, Canada
[14] Université de Nice Sophia–antipolis, CNRS, Observatoire de la Côte d'Azur, Laboratoire Lagrange, BP 4229, F-06304 Nice, France
Received 2021 December 6; revised 2022 April 3; accepted 2022 April 15; published 2022 June 2

Abstract

We present new period-ϕ_{31}-[Fe/H] relations for first-overtone RRL stars (RRc), calibrated over a broad range of metallicities ($-2.5 \lesssim$ [Fe/H] $\lesssim 0.0$) using the largest currently available set of Galactic halo field RRL with homogeneous spectroscopic metallicities. Our relations are defined in the optical (ASAS-SN *V* band) and, inaugurally, in the infrared (WISE *W1* and *W2* bands). Our *V*-band relation can reproduce individual RRc spectroscopic metallicities with a dispersion of 0.30 dex over the entire metallicity range of our calibrator sample (an rms smaller than what we found for other relations in literature including nonlinear terms). Our infrared relation has a similar dispersion in the low- and intermediate-metallicity range ([Fe/H] $\lesssim -0.5$), but tends to underestimate the [Fe/H] abundance around solar metallicity. We tested our relations by measuring both the metallicity of the Sculptor dSph and a sample of Galactic globular clusters, rich in both RRc and RRab stars. The average metallicity we obtain for the combined RRL sample in each cluster is within ± 0.08 dex of their spectroscopic metallicities. The infrared and optical relations presented in this work will enable deriving reliable photometric RRL metallicities in conditions where spectroscopic measurements are not feasible; e.g., in distant galaxies or reddened regions (observed with upcoming Extremely Large Telescopes and the James Webb Space Telescope), or in the large sample of new RRL that will be discovered in large-area time-domain photometric surveys (such as the LSST and the Roman space telescope).

Unified Astronomy Thesaurus concepts: RR Lyrae variable stars (1410); RRc variable stars (1415); Pulsating variable stars (1307); Globular star clusters (656); Metallicity (1031)

Supporting material: machine-readable table

1. Introduction

RR Lyræ stars (RRL hereafter) are a ubiquitous and widely used tracer of old (age >10 Gyr, Walker 1989; Savino et al. 2020) stellar populations in the Milky Way (MW) and Local Group (LG) galaxies (see, e.g., MW: Matteucci 2021, Carina: Coppola et al. 2015; Sculptor: Martínez-Vázquez et al. 2016a; M31 dwarf satellites: Martínez-Vázquez et al. 2017; Monelli et al. 2017; isolated LG dwarfs: Bernard et al. 2009, 2010, 2013). Their relevance has become even more important in the current age of large-area photometric time surveys (e.g., ASAS-SN: Shappee et al. 2014; Jayasinghe et al. 2018; the Catalina Sky Survey: Drake et al. 2009; Pan-STARRS: Chambers et al. 2016; DES: Abbott et al. 2018; Gaia: Clementini et al. 2016, 2019; TESS: Ricker et al. 2015), which have significantly increased the number of known RRL variables. An even larger number of these variables is expected to be discovered as the product of upcoming next-generation surveys, such as the Vera C. Rubin Observatory Legacy Survey of Space and Time (LSST; Ivezić et al. 2019) in the optical, and surveys that will be executed for the Nancy Grace Roman telescope (Akeson et al. 2019) at near-infrared wavelength.

The importance of RRL as tracers is related to their role as distance indicators. Period-Wesenheit-metallicity relations (PWZ) in the optical and period-luminosity-metallicity relations (PLZ) in the infrared (theoretical: Marconi et al. 2015; Neeley et al. 2017; and observational: Dambis et al. 2013; Muraveva et al. 2018; Neeley et al. 2019; Gilligan et al. 2021) now provide individual RRL distances with an accuracy approaching other traditional stellar standard candles that can be characterized by a Leavitt law (Leavitt 1908; Leavitt & Pickering 1912), such as Cepheids.

In the case of classical (Population I) Cepheids, the metallicity dependence on luminosity may, in most cases, be ignored (but see, e.g., Breuval et al. 2021); however, the much larger spread in metallicity for RRL (Population II stars) requires reliable measurements of their [Fe/H] abundance to provide accurate distances. Having metallicity measurements available can be a challenge because they are traditionally derived with spectroscopic methods, and spectra cannot be expected to be readily available for the large sample of variables that are being discovered in large-area surveys. This can be due to logistical constraints based upon telescope time or physical limitations for taking spectra, such as extreme distances or high extinction in environments that can only be probed photometrically by mid-infrared cameras. A reliable and precise method for extracting physical parameters based solely on photometric time series is necessary to keep pace with this expansion.

Simon & Lee (1981) first showed for variable stars that specific physical parameters, such as metallicity, could be directly related to a light curve's shape (characterized through its Fourier decomposition). Jurcsik & Kovacs (1996) quantified this relationship by finding a bilinear relation between period and a low-order Fourier phase parameter ($\phi_{31} = \phi_3 - 3 \cdot \phi_1$) derived in the optical for RRLs pulsating in the fundamental mode (also known as RRab). Additional works have analyzed and revised this relation for RRab (Nemec et al. 2013; Martínez-Vázquez et al. 2016; Smolec 2005; Ngeow et al. 2016; Iorio & Belokurov 2020; Mullen et al. 2021) using more modern data sets in a variety of wavelengths. In particular, Mullen et al. 2021 (hereafter Paper I) obtained a new relation in the V band based on the largest RRab calibration data set to date. In Paper I, we showed that accurate RRab photometric metallicities could be extended to both lower and higher metallicity regimes than in previous works. Furthermore, for the first time, we showed that a photometric metallicity relation for RRab variables could be extended into the mid-infrared. This paper aims to now derive similar relations for RRL pulsating in the first overtone (RRc variables).

The study of RRc variables possesses additional challenges with respect to RRab. An important issue is the sample size, as the number of RRc is only $\sim 1/3$ of all field RRL (the ratio of RRc to the total number of RRL is intimately tied to how [Fe/H] affects the horizontal branch morphology; Fabrizio et al. 2021). Furthermore, extracting accurate periods and Fourier parameters for RRc often takes an additional layer of scrutiny stemming from their inherent smaller amplitudes and quasi-sinusoidal light curves when compared to the characteristic high-amplitude saw-tooth shape RRab, which are more strongly dependent on atmospheric abundances. Due in part to these issues, it was not until Morgan et al. (2007; hereafter M07) that it was shown that similar period-ϕ_{31}-[Fe/H] equations could be made for RRc in the V band. Further work by Nemec et al. (2013; hereafter N13), Morgan (2014; hereafter M14), and Iorio & Belokurov (2020; hereafter IB20) extended this analysis to well-sampled RRc light curves obtained with the Kepler space telescope (Koch et al. 2010), to a revised sample of globular clusters (GC) with V-band photometry, and by using Gaia DR2 (Gaia Collaboration et al. 2018; Holl et al. 2018; Clementini et al. 2019) G-band light curves, respectively.

Due to the scarcity of accurate high-resolution ($R \gtrsim 20{,}000$) spectroscopic metallicity measurements (capable of providing an accuracy of $\sim$0.1 dex in [Fe/H]) for individual RRc, these relations have all been predominantly based on RRc residing in globular clusters (GCs) with well-studied cluster metallicity. In this work, we leverage newly determined RRc high-resolution (HR) metallicities from Crestani et al. (2021a; C21 hereafter). We combine these measurements with a large sample of metallicities derived with medium-resolution spectroscopic surveys ($R \sim 2000$). This new set of medium-resolution metallicities has been derived with the updated C21 calibration of the ΔS method (Preston 1959), which relies on ratios of the equivalent widths of the Ca and H lines. While not as accurate as HR metallicities, this method can nevertheless provide reliable [Fe/H] abundances with a typical uncertainty of 0.2–0.3 dex.

This work directly follows the analysis presented in Paper I for the calibration of period-ϕ_{31}-[Fe/H] relations for RRab field stars. We take advantage of an extensive catalog of field RRc [Fe/H] abundances from C21 HR spectral measurements, combined with ΔS metallicities estimated from large publicly available medium-resolution spectral data sets. We then cross-correlate this extensive HR+ΔS metallicity catalog with well-sampled archival light curves in order to derive novel period-ϕ_{31}-[Fe/H] relations for RRc in the optical (V-band) and, for the first time, in the mid-infrared ($W1$ and $W2$ bands). Our work shows that these relations can indeed be extended to the thermal infrared, where the light curves are determined mainly by the radius variation during the star's pulsation rather than by the effective temperature changes that dominate in the optical wavelengths. This will be crucial to allow the determination of reliable metallicities in upcoming space infrared surveys, such as the James Webb Space Telescope (JWST; Gardner et al. 2006).

This paper is structured as follows. In Section 2 we describe the data sets we adopt for our work: the HR+ΔS metallicity catalog utilizing the work of C21 and the optical and infrared time-series catalogs from which we derived the RRc light curves. In Section 3 we explain how our period-ϕ_{31}-[Fe/H] relations are calibrated. We then validate our sample to remove contaminants such as eclipsing contact binaries, which possess similar light curves to RRc and can often be misclassified. Our results are discussed in Section 4, where we assess the precision of the optical and infrared relations, compare our relations with previous ones found in literature, and apply our method to measure the [Fe/H] abundance in a sample of globular clusters. Last, we derive the metallicity distribution of the MW dwarf spheroidal (dSph) satellite Sculptor and compare it to the metallicities available using other solely photometric methods. Our conclusions are presented in Section 5.

2. First-overtone RR Lyrae Data Sets

Our sample of RRLs is derived from an extensive catalog of 3057 field RRc, for which we have either [Fe/H] abundances derived from HR spectra (40 sources) or an estimate of their metallicity based on the ΔS method (3017 sources). In order to ensure a homogeneous metallicity scale for our entire sample, both HR and ΔS metallicities are based on the calibration provided in C21 (in turn consistent with the Carretta et al. 2009 metallicity scale). The RRc stars for which we obtained ΔS metallicities were extracted from both the full Large Scale Area Multi-Object Spectroscopic Telescope (LAMOST) DR2 survey (Deng et al. 2012; Liu et al. 2014) and the Sloan Extension for Galactic Understanding and Exploration (SEGUE; Yanny et al.

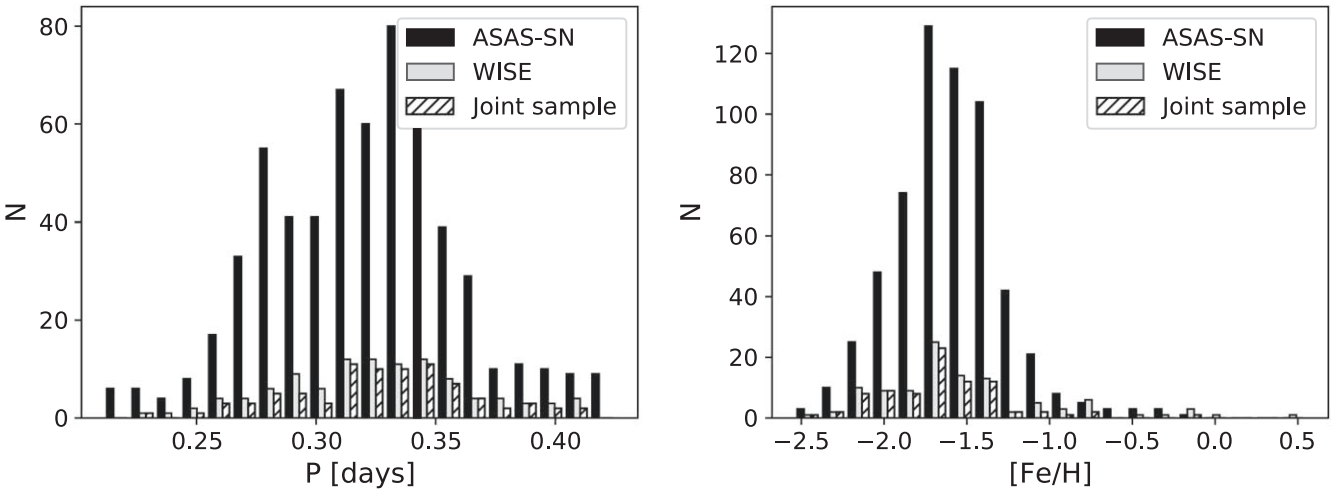

Figure 1. Period distribution (left) and spectroscopic [Fe/H] distribution (right) of the different calibration data sets. The histogram labeled "Joint sample" (hatched) corresponds to the stars in common between the ASAS-SN (optical *V* band, in black) and WISE (infrared *W1* and/or *W2* bands, in gray) data sets.

Table 1
Calibration Data Sets

	ASAS-SN	WISE		Joint Sample
Bands	*V*	*W1*	*W2*	*V*, (*W1* or *W2*)
RRc stars	594	106	71	83
Period in days (range)	0.21–0.43	0.23–0.41	0.24–0.41	0.23–0.41
Period in days (median value)	0.32	0.32	0.32	0.33
[Fe/H] (range)	−2.54–(−0.16)	−2.54–0.55)	−2.54–(+0.06)	−2.54–(−0.16)
[Fe/H] (median value)	−1.60	−1.64	−1.65	−1.66
Number of epochs (range)[a]	118–835	159–2942	159–2942	⋯
Number of epochs (median value)	230	205	212	⋯
Magnitude (range)	9.12–16.63	8.10–13.01	8.12–12.75	⋯

Note.
[a] The number of epochs is recorded prior to removing any spurious photometric measurement (see Section 3.1).

2009) survey data sets. For a complete and detailed description of the metallicity scale, the HR metallicity catalog's demographics, the ΔS calibration, and the spectrum selection criteria, we refer to the C21 paper.

We have then cross-matched the variables in our HR+ΔS metallicity catalog with well-sampled photometric time series in the All-Sky Automated Survey for Supernovae (ASAS-SN; Shappee et al. 2014; Jayasinghe et al. 2018) and the Near-Earth Objects reactivation mission (NEOWISE; Mainzer et al. 2011) of the Wide-field Infrared Survey Explorer (WISE; Wright et al. 2010). From the ASAS-SN survey, we extracted 594 good-quality ASAS-SN RRc light curves in the *V* band. Similarly, from the WISE/NEOWISE missions, we obtained 106 good-quality infrared light curves in at least one of the available bands. Individually, the *W1* (3.4 μm) and *W2* (4.6 μm) bands had 106 and 71 good-quality RRc stellar light curves, respectively. From now on, the combination of photometry from both the primary WISE and ongoing NEOWISE mission are referred to for brevity as WISE. Table 1 lists the properties of the RRc in our calibration samples that have passed the stringent photometric and Fourier decomposition criteria described in Section 3. The *Joint Sample* column denotes the subset of 83 RRc for which both optical and infrared light curves are available.

Figure 1 shows the distribution of period and metallicity for the optical (ASAS-SN) and infrared (WISE) calibration samples and the stars in common (joint). All samples cover the entire period range expected for RRc variables and are representative of the metallicity of Galactic halo RRLs, with a median [Fe/H] abundance of ≈ -1.6 in both the ASAS-SN and WISE samples. The broad range of metallicities apparent in Figure 1 ensures ample leverage for calibrating our period-ϕ_{31}-[Fe/H] relations.

The apparent magnitude distribution of the calibration data sets is shown in Figure 2 for the *V* band (left panel) and *W1* band (right). The histogram for the *W2* band is similar, but contains fewer stars due to the lower sensitivity in this band, resulting in generally noisier light curves. The joint sample (hatched in both panels) is noticeably truncated at $V \sim 14$ mag due to the WISE survey's shallower photometric depth.

3. Calibration of Period–Fourier–Metallicity Relation

3.1. Data Processing

The extraction of period and Fourier parameters directly follows the procedure outlined in Paper I, Section 3, and is summarized below. We first refine the period of each variable with the Lomb-Scargle method (Lomb 1976; Scargle 1982), applied to the large temporal baseline (>8 yr) of the ASAS-SN and WISE time-series data. A Gaussian locally weighted regression smoothing algorithm (GLOESS; Persson et al. 2004) is then applied to the phased data in order to smooth over

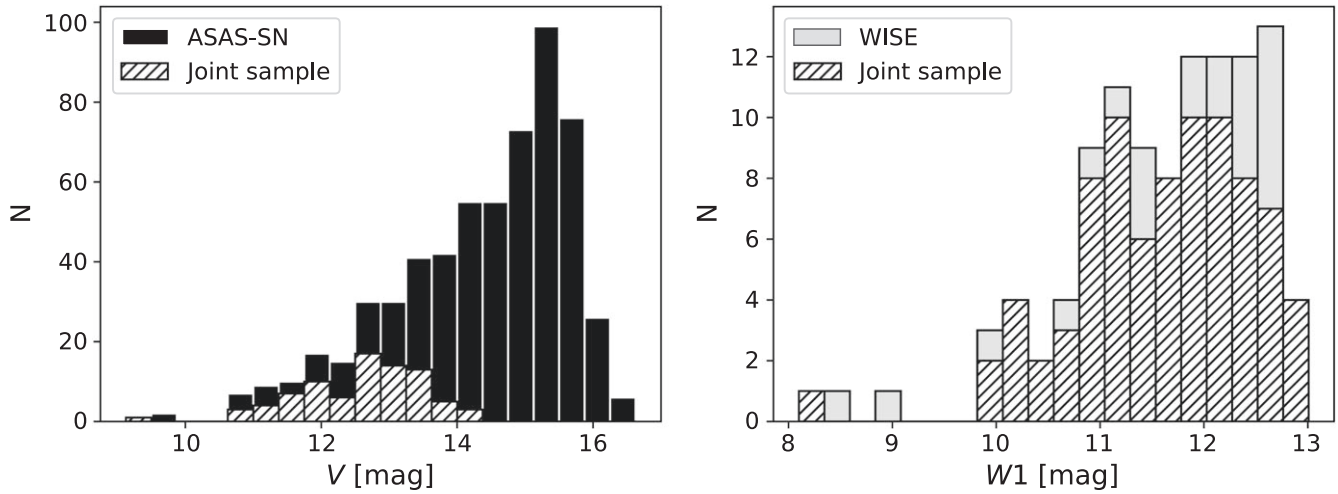

Figure 2. Distribution of the average *V*-band apparent magnitude (left) and the average *W1*-band apparent magnitude (right). Each panel shows both the entire calibration sample (solid filled) and the joint sample (hatched filled) subset of stars having both ASAS-SN and WISE data.

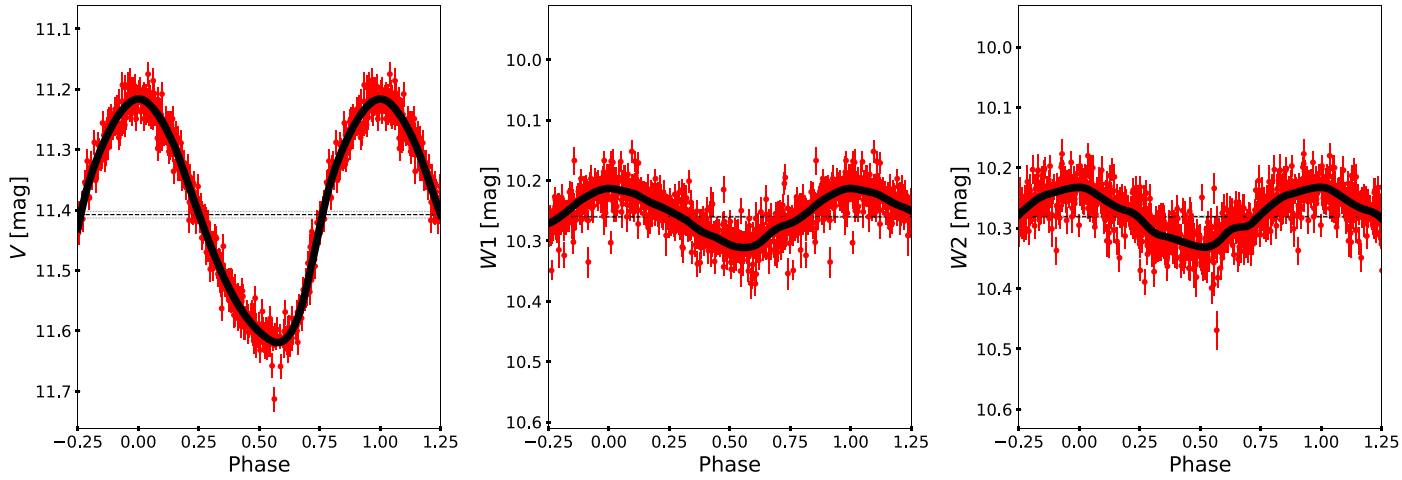

Figure 3. Multiple-band light curves for a typical RRc star. The *V* (left), *W1* (middle), and *W2* bands (right) are shown for the star XX Dor (Period = 0.32894 days). The Fourier fit (solid black line) to the GLOESS light curve (see text) is plotted on top of the phased data (red). The average magnitude with its associated error is shown as horizontal black dotted lines. Points automatically rejected by the GLOESS fitting procedure have been removed.

unevenly sampled data and exclude outliers. A Fourier sine or cosine decomposition is finally executed on each GLOESS light curve by applying a weighted least-squares fit of the following equation (in the case of the sine decomposition):

$$m(\Phi) = A_0 + \sum_{i=1}^{n} A_i \sin[2\pi i(\Phi + \Phi_0) + \phi_i], \qquad (1)$$

where $m(\Phi)$ is the observed magnitude for either the ASAS-SN or WISE bands, A_0 is the mean magnitude, n is the order of the expansion, Φ is the phase from the GLOESS light curve varying from 0 to 1, Φ_0 is the phase that corresponds to the time of maximum light T_0, and A_i and ϕ_i are the ith order Fourier amplitude and phase coefficients, respectively. A similar equation can be written to represent the equivalent cosine decomposition. For RRc, n is often lower than five; however, we advise choosing the optimal number of terms for the data set with care (see Petersen 1986; Deb & Singh 2009) as the addition of higher-order terms may cause inconsistencies in the value of low-order Fourier parameters. For this work, we note that by using an intermediate GLOESS step to eliminate noise factors, the Fourier parameters are consistent between third-, fourth-, or fifth-order decompositions, with the exclusion of a small number of $\gg 3\sigma$ outliers ($\sim$4% of total RRc for ASAS-SN and $\sim$8% for WISE). This small subset of outliers has been excluded in our processing to make our result invariant between different decomposition orders used. However, it is worth noting that with the robust fitting procedure outlined in Section 3.3, the results of this paper remain unaltered with the inclusion or exclusion of these sources. Figure 3 shows a typical *V*, *W1*, and *W2* light curve from our RRc calibration stars, where the Fourier decomposition fit (solid black line) is plotted on top of the actual photometric data in red.

As in Paper I, we explore the link between metallicity and Fourier coefficients through either the ratios of Fourier amplitudes $R_{ij} = A_i/A_j$, or the linear combinations of the phase coefficients $\phi_{ij} = j \cdot \phi_i - i \cdot \phi_j$, where ϕ_{ij} is cyclic in nature and ranges from 0 to 2π. This is shown in Figure 4, where several low-order Fourier parameters of individual RRc stars are plotted against period and color-coded based on their [Fe/H]. In the case of the RRc *V*-band ϕ_{31} values (top right), it is advantageous to represent the phase parameter as a product of a

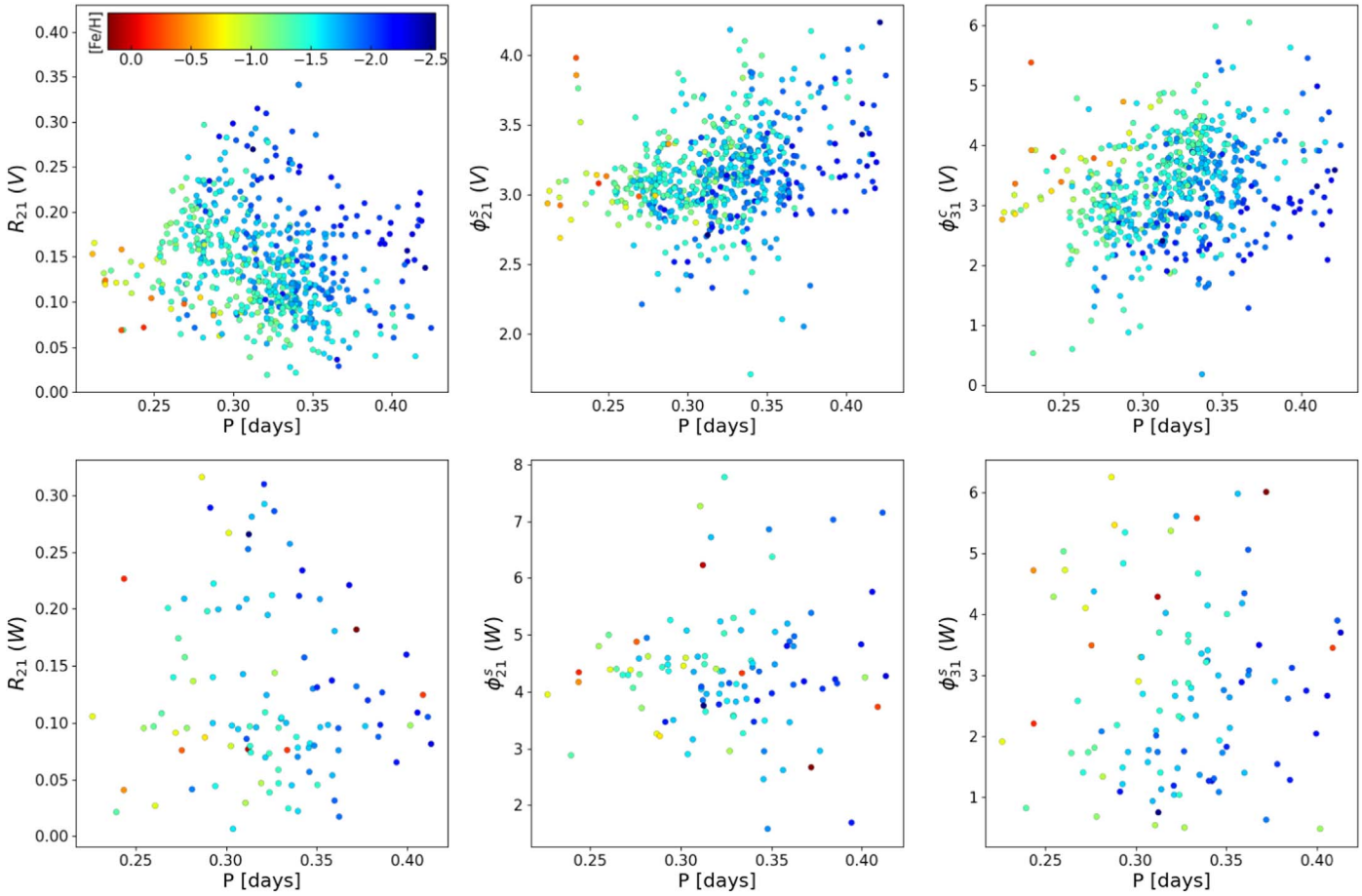

Figure 4. ASAS-SN *V*-band (top row) and *W1*-band (bottom row) Fourier parameters as functions of the period. RRLs are color-coded based on their spectroscopic calibration metallicities. In the rightmost column (ϕ_{31}), [Fe/H] generally goes from metal-rich in the left (red) to metal-poor in the right (blue). All parameters have been derived with a sine Fourier decomposition (indicated with a *s* superscript), except for the top right panel ($\phi^c_{31}(V)$ values) where the Fourier phase parameters have been converted into a cosine decomposition (see text). Average errors for each of the parameters plotted are smaller than the size of the data points.

cosine decomposition rather than sine to avoid the rollover of the ϕ_{31} parameter across the 2π boundary. This can be achieved by either adopting the cosine form of Equation (1) or using the simple transformation $\phi^c_{31} = \phi^s_{31} - \pi$ between the sine (*s* superscript) and cosine (*c* superscript) form of this parameter.

In all *V*-band panels, we can readily see a gradient in the [Fe/H] distribution of the stars. We found the most distinct separation to be in the ϕ^c_{31} versus period plot, confirming earlier studies, such as M07, which suggests that a relation between period and ϕ^c_{31} is a good indicator of metallicity for the *V*-band RRc. We similarly found that the ϕ^s_{31} versus period plot for WISE (bottom right panel) showed the most distinct trend with metallicity. However, the general metallicity trends in the WISE bands are less apparent than in the optical due to both the smaller sample size and the larger intrinsic dispersion of ϕ_{31} values, covering almost the entire 2π range. As in the case of the RRab stars, we take advantage of the nearly identical shape of the light curves in the *W1* and *W2* bands (see, e.g., Figure 3) to improve the signal in the WISE Fourier parameters by averaging the $\phi^s_{31}(W1)$ and $\phi^s_{31}(W2)$ values for stars with both light curves available. See Paper I, Section 3.2 for a quantitative discussion demonstrating the validity of this approach for the RRab stars; we have verified that this result still holds for our RRc sample.

3.2. Eclipsing Contact Binary Contamination

Upon initial creation of our ΔS metallicity sample, we found a significant population of stars that were previously marked as RRc in the literature, but were found on further analysis to be likely eclipsing contact binaries known as W Ursae Majoris (W UMa). These binaries have sinusoidal light curves similar to RRc variables, and can be confused with first-overtone RRL stars if they happen to have a similar period and amplitude. If the noise is high enough in a W UMa light curve, it can prevent detection of a characteristic secondary eclipse.

Indeed, we found that for our sample of W UMa, most combinations of Fourier parameters show some degree of degeneracy with regions typical of RRc. In particular, Figure 5 shows that some W UMa binaries largely overlap with RRc variables in the optical Bailey diagram, although their amplitude tends to be smaller. The overlap is partially mitigated in the infrared (*W1*, shown in the figure, or *W2* diagrams), in which case the same W UMa tends to have larger amplitudes than RRc with a similar period. This opposite trend of amplitudes with wavelengths provided us with a simple criterion to automatically identify and reject the W UMa binaries from our sample in the case both bands are available (as in our joint sample): as shown in the left panel of Figure 5,

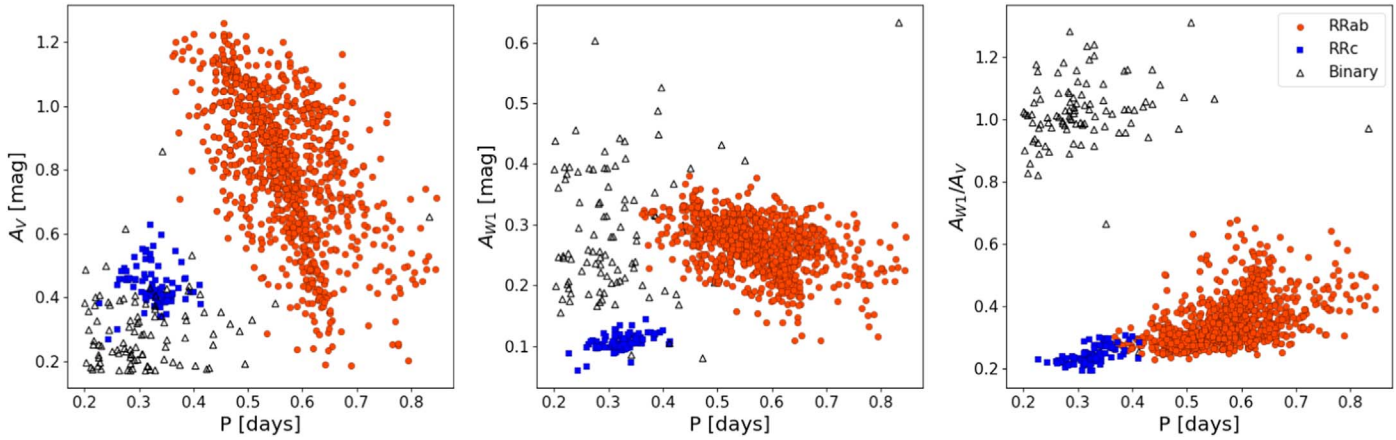

Figure 5. Period vs. amplitude diagram for the ASAS-SN *V* band (left) and the WISE *W1* band (middle). The right panel shows the ratio of the *W1* to *V* amplitudes. The data plotted represent the subset of stars for which both optical and infrared are available, i.e., the RRc joint sample discussed in Section 2 (blue squares), the RRab joint sample (red circles) from Paper I, and eclipsing contact binary contaminants selected as explained in Section 3.2 (empty triangles).

the A_{W1}/A_V ratio provides a clear separation between RRc stars and the potential binaries.

For all sources with only one available light curve (either in the optical or infrared), we resorted to less reliable criteria and manual inspection of the light curves. These criteria were developed for individual bands by analyzing an initial sample of the potential W UMa that have been identified with their amplitude ratio between the infrared and optical. If only the *V*-band photometry was available, we flagged as potential W UMa all sources with $A_V \lesssim 0.15$ or $\phi_{21}^s(V) > 4.25$. For stars with infrared data alone, we instead flagged all stars with $A_W > 0.15$ (in either the *W1* or *W2* bands, depending on availability). We then visually examined the phased light curve in the one available band, searching for a secondary light curve minimum, which could have been missed in previous work based on less detailed photometry. We then rejected all sources showing evidence of such secondary eclipses.

The analysis presented in this paper (including Table 1) focuses solely on this sample, which has been cleaned of W UMa. We provide the final cautionary note that certain W UMa as shown can be easily misconstrued as RRc, and anyone using the relations published in this work should take extreme care in the validity of their RRc sample.

3.3. Period–Fourier-[Fe/H] Fitting

As discussed in Section 1, RRc photometric metallicities based on a Fourier decomposition of optical light curves are available for different literature relations (see, e.g., M07, N13, M14, and IB20). These relations are either linear in both period and ϕ_{31} or use higher-order combinations of these two parameters. Our tests show that, for our sample, higher-order and nonlinear terms in the period, ϕ_{31}, or other Fourier parameters result in minimal benefits at the expense of complexity and decreased robustness in the fitting results. For these reasons, we decided to proceed using a simple linear relation in period and ϕ_{31}, similarly to what we did in Paper I for the RRab stars.

To validate this choice of a period-ϕ_{31} plane fit, we followed the methodology described in Appendix B of Paper I. Principal component analysis showed that 91.30% of the variance in the *V*-band RRc data could be attributed to just two principal axes (i.e., a plane). This is comparable to the 92.9% value we found for RRab stars in Paper I, which we interpreted as suggesting that a third fit parameter was not needed. A similar analysis for the infrared RRc data set showed that 85.17% of the variance could be attributed to two dimensions (6.74% less than what we found for the RRab in the WISE bands). We attribute this larger variance to a larger relative scatter in the WISE data set itself (seen in the bottom right panel of Figure 4) due to the smaller amplitude of the pulsations, higher intrinsic photometric noise in the data, and smaller size of the sample. Search for a third observable parameter and/or higher-order fitting functions did not result in a better fit, leading us to adopt a period-ϕ_{31} plane fit for the infrared data set as well.

We initially attempted to fit an RRc period-ϕ_{31}-[Fe/H] relation adopting the same procedure as described in Paper I. We quickly discovered that the smaller size of the RRc sample (by a factor of 3 and 10, compared to the RRab, in the ASAS-SN and WISE bands, respectively) resulted in a fit that was highly dependent upon the exact calibration sample used. Bootstrap analysis (Efron & Tibshirani 1986) highlighted that this instability in the fitting results was due to a combination of higher susceptibility to individual outliers and a stronger correlation between the period and ϕ_{31} slopes. We found, however, that when different bootstrap samples were used, the range of period slopes we obtained for the best-fit RRc relation was consistent with the value we derived in Paper I for the RRab relation. Based on these considerations, we decided to freeze the period slope of the RRc period-ϕ_{31}-[Fe/H] relation to the RRab value, effectively reducing the RRc fit to a two-parameter fit in the metallicity zeropoint *a* and the ϕ_{31} slope *c*,

$$[\mathrm{Fe/H}] = a + b_F \cdot (P_F - P_0) + c \cdot (\phi_{31} - \phi_{31_0}), \qquad (2)$$

,where b_F is the period slope from the fit of RRab stars in Paper I, equal to -7.60 ± 0.24 dex/ day^{-1} for the ASAS-SN *V* band, and -8.33 ± 0.34 dex/ day^{-1} for the WISE bands. Note that for this choice of values to be appropriate, the period of the RRc variables needs first to be "fundamentalized", or transformed into its equivalent fundamental period by using the equation $\log P_F = \log P_{FO} + 0.127$ (Iben & Huchra,J 1971; Rood 1973; Cox et al. 1983). Fundamentalizing the period of overtone pulsators is a common technique when deriving PLZ and PWZ relations of Cepheids and RRL variables (see, e.g., Groenewegen 2018; Marconi et al. 2015; Neeley et al. 2015) when their smaller number and narrower period range makes it

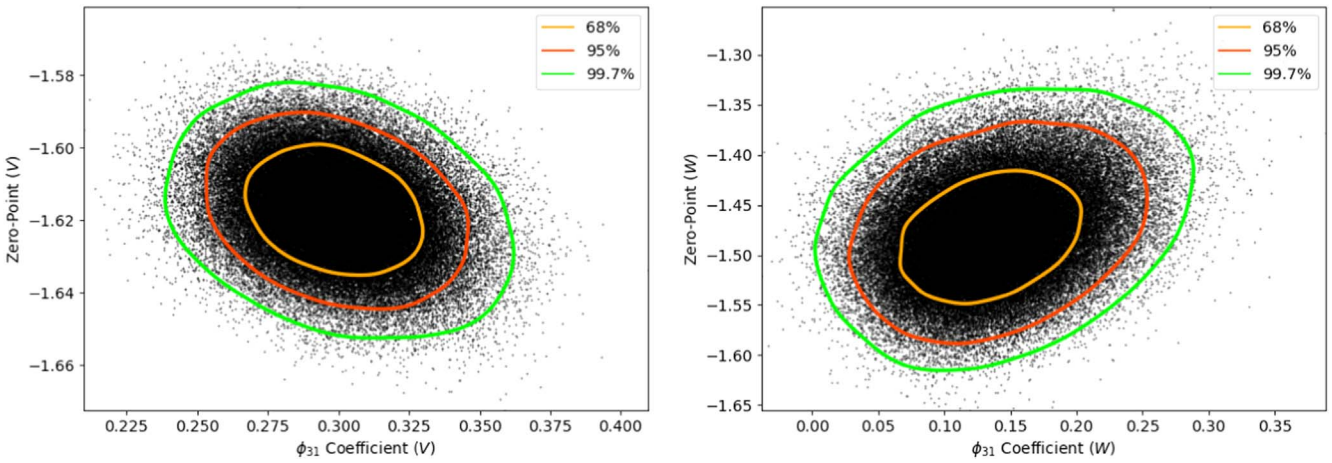

Figure 6. Fitting parameters from the bootstrap resampled ODR method applied to the ASAS-SN (V) sample, left, and WISE (W) sample, right. Contours denote regions containing 68% (red), 95% (orange), and 99.7% (green) of the sampled parameters.

prohibitive to fit them alone. It is worth noting that fundamentalization does have a minor dependence upon metallicity (Bragaglia et al. 2001; Soszyński et al. 2014); however, the effect is so small that regardless of the relation tried (e.g., Coppola et al. 2015), the results of this paper remain unchanged. Finally, as in Paper I, we have included the pivot offsets P_0 and ϕ_{31_0} to add further robustness to the fitting procedure; each value is close to the median of the period and [Fe/H] distribution for the RRc sample.

We fit the two remaining free parameters of Equation (2), and their uncertainties using an orthogonal distance regression (ODR) routine combined with bootstrap resampling. The analysis we presented in Paper I for RRab stars showed that ODR tends to minimize trends along all fitted dimensions as no differentiation is made between dependent and independent variables. The ODR fit was run multiple times using bootstrap resampling, where in each run, all the parameters of each individual calibrator star (period, ϕ_{31}, and [Fe/H]) are randomly replaced with all the corresponding parameters from any singular star in the same calibration data set. Namely, we are sampling with replacement our entire calibration data set before fitting our relation, and ensuring each resampled calibration data set is the same size as our initial sample. Note that all the stars in our calibration sample are fitted with equal weight, as the uncertainties in the fit are dominated by the intrinsic scatter we observe in the period-ϕ_{31}-[Fe/H] plane (see Figure 4), in comparison to the small uncertainties in period and the ϕ_{31} parameter ($\sim 10^{-6}$ days and $\sim$0.02 radians on average, respectively).

Figure 6 shows the cloud of best-fit values obtained with the process described above in the optical and infrared fit. The contours enclose the regions with 68%, 95%, and 99.7% of the ODR best-fit values obtained with 100,000 bootstrap resampled data sets. The contours provide a visual representation of the robustness of the fitting parameters with respect to outliers and are significantly larger than the corresponding 1, 2, and 3σ error ellipses of the best-fit parameters of individual ODR fits. For this reason, we adopted the mean values and standard deviations of the bootstrap resampled ODR fits as solutions and uncertainties for our RRc period-ϕ_{31}-[Fe/H] relations,

$$[\mathrm{Fe/H}]_V = (-1.62 \pm 0.01) + (-7.60) \cdot (P_F - 0.43) + (0.30 \pm 0.02) \cdot (\phi_{31}^c - 3.20) \quad (3)$$

$$[\mathrm{Fe/H}]_W = (-1.48 \pm 0.05) + (-8.33) \cdot (P_F - 0.43) + (0.14 \pm 0.05) \cdot (\phi_{31}^s - 2.70) \quad (4)$$

where Equations (3) and (4) provide photometric metallicities for the ASAS-SN V band and WISE $W1$ and $W2$ infrared bands (averaged when possible; see Section 3.1). Note again how the V-band metallicities are expressed as a function of the cosine decomposition of the optical light curves (i.e., they depend on ϕ_{31}^c), while the WISE formula is a function of the sine decomposition parameter ϕ_{31}^s.

Figure 6 and the uncertainties quoted in Equations (3) and (4) show that the sampled coefficients occupy a much smaller region of the parameter space in the V band than in the W band. The larger uncertainties in the infrared coefficients are a reflection of the larger intrinsic scatter we noted in the W-band period-ϕ_{31}-[Fe/H] plane (Figure 4) as well as a consequence of the smaller size of the infrared calibrator sample. A detailed analysis of the performance of these relations is provided in Section 4. Table 2 lists the derived photometric properties for both the V-band and infrared data sets, including the period, ϕ_{31} value, and photometric metallicity derived in each band with Equations (3) and (4).

4. Discussion

4.1. Comparison with Globular Cluster Metallicity

In order to test the V-band relation obtained in Section 3.3 on an independent sample, we selected a list of 10 GCs with metallicity homogeneously spread between [Fe/H] = −1.0 and −2.3 dex. The clusters we sampled are the same as in Paper I, with two additional GCs: Reticulum (a Large Magellanic Cloud GC), and NGC 6171. Photometry of the clusters comes from Piersimoni et al. (2002; NGC 3201), Kuehn et al. (2013; Reticulum), M14 (NGC 6171), and the homogeneous data set of P. B. Stetson[15] (hereafter PBS) for the remaining majority.

The general properties of the clusters are listed in Table 3, which includes their spectroscopic metallicities (in the scale of C09) and the number of RRL with good-quality well-sampled light curves available in each cluster. The spectroscopic metallicity of the Galactic GCs are obtained from C09,

[15] https://www.canfar.net/storage/list/STETSON/homogeneous/Latest_photometry_for_targets_with_at_least_BVI

Table 2
Derived Photometric Properties of the RRc Sample

Gaia ID (DR3)	Period[a] (day)	ϕ_{31}^{c} (V) (radian)	$\sigma_{\phi_{31}}$ (V) (radian)	$[Fe/H]_V$ (dex)	ϕ_{31}^{s} (W) (radian)	$\sigma_{\phi_{31}}$ (W) (radian)	$[Fe/H]_W$ (dex)
6914532141197318784	0.334879	5.002	0.017	−1.22			
6913110953698726912	0.324371	3.180	0.008	−1.66			
6910854717182648448	0.323513	4.150	0.013	−1.36			
6897117354482002688	0.322392	3.418	0.007	−1.57			
6731321171497007488	0.223019	2.917	0.005	−0.71			
6688916306549500800	0.339563	3.588	0.004	−1.69	3.244	0.041	−1.61
6340460627660385920	0.285073	2.725	0.004	−1.39			
6340096929829777152	0.384128	4.077	0.011	−2.00	2.619	0.007	−2.19
6307501113055775232	0.339337	3.149	0.009	−1.82			
6299550445690958080	0.296671	3.944	0.004	−1.15			

[a] When both V-band and infrared (WISE) data are present, the period included was calculated from ASAS-SN (V-band) data as the period is usually more accurate due to the higher amplitude and steeper light curve. Period accuracies are quoted to an accuracy on the order of 10^{-6} days, corresponding to a readily detectable ∼1% shift in phase for a typical 0.32 -day period RRc star when phased over the large temporal (>8 yr) baseline of our data sets.

(This table is available in its entirety in machine-readable form.)

while the metallicity of Reticulum is from Mackey & Gilmore (2004) and converted from the [Fe/H] scale of Zinn & West (1984, ZW84) to C09. A Fourier decomposition was performed on each light curve to obtain their ϕ_{31} parameters, with the exception of the stars in NGC 6171 and NGC 3201, for which the Fourier parameters were taken directly from their respective photometric catalogs. The period-ϕ_{31}-[Fe/H] relations for RRc (Equation (3)) and RRab (Equation (6) from Paper I with [Fe/H] shifted to the scale of C09) were then applied to estimate the metallicity of each RRL star in the clusters. Note that no metallicity scale corrections are needed between that of C09 and the RRc relations presented in this work. The average [Fe/H] abundance of the RRc and RRab variables in each cluster, with their standard deviation, are listed in columns 4 and 6 of Table 3, respectively.

Figure 7 shows the spectroscopic [Fe/H] versus the mean photometric [Fe/H] values, calculated for each GC with our relations. Each RRab and RRc stellar photometric metallicity measurement contributes equal weight to the mean photometric [Fe/H] for a given GC. The figure, as well as the individual values listed in Table 3, demonstrates the good performance of our formulæ (including the new relations for RRc variables) to provide reliable [Fe/H] abundances. The combination of the photometric RRab metallicities (from Paper I) with the new photometric RRc metallicities is in good agreement with the spectroscopic metallicities of the clusters: overall ±0.08 dex, which is well within the respective uncertainties.

4.2. Comparison with Literature Relations

In this section, we compare photometric metallicities derived using a variety of period-ϕ_{31}-[Fe/H] relations, including those found in this work (Equations (3) and (4)), as well as the fits provided by M07, M14, N13, and IB20. Figure 8 shows the photometric metallicities for all the RRc in our calibration sample, plotted as a function of their spectroscopic [Fe/H] abundances. The rms scatter of each relation, calculated with respect to the ideal one-to-one relation over the entire spectroscopic metallicity range within which each relation has been calibrated, is indicated in each case.

The top row shows the analysis of our fits in the optical (ASAS-SN, left) and infrared (WISE, right) bands. Since we are directly comparing to the same sample used to derive these relations, the figure allows us to check for remaining trends in the residuals with respect to the ideal one-to-one relation to ensure that our relations provide a consistent estimate of each star's [Fe/H] over the entire metallicity range of our calibration sample. For the case of the V-band ASAS-SN data set, we show nearly symmetric residuals (with an rms ≈ 0.30 dex) over the entire range of metallicities with only a minor deviation at higher metallicities, still well within the error of our relation. The WISE band residuals, however, show some larger divergence at high metallicity ($[Fe/H] \gtrsim -0.5$), where Equation (4) systematically underpredicts the spectroscopic metallicities. The overall residual rms is also significantly larger (0.50 dex) than the one we obtained in the V band. Due to the small number of high-metallicity RRc stars, we cannot determine if this is due to nonlinearity of the period-ϕ_{31}-[Fe/H] in this metallicity regime or rather a reflection of less accurate spectroscopic metallicities for the stars in our calibration sample that approach solar [Fe/H] abundance. Indeed, Crestani et al. (2021b) found that the RRL that have been used to calibrate the ΔS method in Crestani et al. (2021a), which we in turn use as the basis for our own relation, show a broad dispersion in α-elements measured through high-resolution spectroscopy. Since the ΔS method is based on the strength of a Ca line, while our Fourier-ϕ_{31}-metallicity method aims to measure [Fe/H] metallicities, a spread in α-element abundances can potentially lead to the observed deviations at the ends of the metallicity scale. If we restrict our WISE bands analysis to $[Fe/H] \lesssim -0.5$, we obtain a best-fit relation that is virtually indistinguishable from Equation (4) (because of the much larger number of low-metallicity RRc, and due to the robustness of our bootstrap fit), but with a residual rms equal to 0.29 dex, nearly identical to the one we found for the V band (calculated over the entire metallicity range). By directly comparing the V-band (Equation (3)) and infrared (Equation (4)) photometric metallicities for the RRc in the joint sample, we note that the two sets of metallicities are consistent with each other within their respective uncertainties.

The middle left panel shows the residuals found with the higher-order nonlinear period-ϕ_{31}-[Fe/H] relation of M07 (their Equation 4). Note that M07 published two equations: one based on the [Fe/H] scale of ZW84, and one based on that of Carretta & Gratton (1997). We choose to analyze the latter due to its smaller quoted dispersion and simpler functional

Table 3
Globular Clusters

Clusters	$[Fe/H]_{C09}$	RRc stars	$[Fe/H]_{RRc}$	RRab Stars	$[Fe/H]_{RRab}$
NGC 7078 (M15)	-2.33 ± 0.02	36	-2.29 ± 0.06	64	-2.25 ± 0.04
NGC 4590 (M68)	-2.27 ± 0.04	9	-2.23 ± 0.13	13	-2.14 ± 0.11
NGC 4833	-1.89 ± 0.05	3	-1.92 ± 0.40	11	-1.95 ± 0.11
NGC 5286	-1.70 ± 0.07	8	-1.69 ± 0.21	25	-1.76 ± 0.07
Reticulum	-1.67 ± 0.12	4	-1.74 ± 0.05	22	-1.58 ± 0.03
NGC 3201	-1.51 ± 0.02	2	-1.64 ± 0.40	50	-1.38 ± 0.08
NGC 5272 (M3)	-1.50 ± 0.05	28	-1.54 ± 0.12	175	-1.39 ± 0.08
NGC 5904 (M5)	-1.33 ± 0.02	21	-1.37 ± 0.08	67	-1.41 ± 0.07
NGC 6362	-1.07 ± 0.05	13	-1.22 ± 0.08	18	-1.16 ± 0.06
NGC 6171 (M107)	-1.03 ± 0.02	8	-1.20 ± 0.04	15	-0.81 ± 0.13

form. Their relation was based on 106 RRc stars from 12 GCs with *V*-band Fourier parameters gathered from heterogeneous publications. In order to consistently compare with the HR +ΔS spectroscopic metallicities, we converted the metallicities derived from the M07 relation into that of C09 using the relation $[Fe/H]_{C09} = (1.137 \pm 0.060)[Fe/H]_{CG97} - 0.003$ (provided by C09). A few years later, M14 published an updated version of their *V*-band M07 fit, using the same base of RRc extended to include a total of 163 stars gathered from 19 GCs, with a metallicity scale updated to that of C09. Although they found a slightly different nonlinear period-ϕ_{31}-[Fe/H] functional form, the metallicities predicted by M14 (center right panel in Figure 8) appear to be roughly the same as those provided by M07. Both relations do not appear to have a trend or bias with respect to the spectroscopic metallicities, but they do have a larger rms (0.36 and 0.39 dex, respectively) than our ASAS-SN relation.

N13 provided a nonlinear period-ϕ_{31}-[Fe/H] for the Kepler Space Telescope *Kp* band (their Equation (4)). Due to the small field of view (relative to large-area surveys) of Kepler's primary mission, this relation is calibrated by augmenting the sample of 3 RRc obtained in Kepler's field with the Fourier parameters of 98 GC RRc from M07, converted into the *Kp* system using the relation $\phi_{31}(V) = \phi_{31}(Kp) - (0.151 \pm 0.026)$ from Nemec et al. 2011. We use this same relation to convert the *V*-band ϕ_{31} parameters of our spectroscopic sample into the *Kp* photometric system in order to generate the bottom left panel of Figure 8. The plot shows that the N13 largely predicts the [Fe/H] metallicities without noticeable trends even outside their [Fe/H] calibration range, albeit with a small negative bias (the average metallicity predicted by N13 is 0.26 dex lower than the spectroscopic values), and a larger scatter (RMS = 0.52 dex) than all other relations evaluated here.

Finally, IB20 used a sample of 50 GC RRc stars extracted from the Gaia DR2 database to derive a bilinear period-ϕ_{31}-[Fe/H] relation (Equation (4) in their paper) with the same functional form as our Equations (3) and (4). In order to apply this relation to our data set, we had to perform two transformations: (1) we converted the *V*-band ϕ_{31} value of our ASAS-SN sample into the *G*-band system using the relation $\phi_{31}(G) = (0.104 \pm 0.020) + (1.000 \pm 0.008)\,\phi_{31}(V)$ from Clementini et al. (2016), and (2) we transformed the metallicity provided by the IB20 relation (in the ZW84 scale) into the Carretta scale using the $[Fe/H]_{C09} = 1.105[Fe/H]_{ZW84} + 0.160$ relation from C09. The results are shown in the bottom right panel of Figure 8. Again, no obvious trend or offset is found, and the rms dispersion (0.32 dex) is among the smallest of the relations assessed in this section, comparable to the rms we measure in the *V* band with our Equation (3).

Overall, M07, M14, and N13 share the majority of their photometric calibration data sets, but differ in their functional form by adding slightly different combinations of nonlinear terms. Figure 8 shows that with respect to optical linear relations (IB20 and Equation (3) in this work), these nonlinear relations tend to have a larger residual dispersion for our large sample of spectroscopic metallicities. With the exception of the infrared WISE band (where we observe a possible departure at solar metallicities), our data set does not support the need for the addition of nonlinear terms in photometric metallicity relations based on the Fourier parameters of RRc optical light curves.

4.3. Comparison with the Sculptor dSph Metallicity

In this section, we test our *V*-band period-ϕ_{31}-[Fe/H] relations with RRL stars in the MW dSph satellite Sculptor. We compare our photometric Fourier metallicities to those derived by Martínez-Vázquez et al. (2016b; hereafter MV16b) by inverting the theoretical PLZ relation from Marconi et al. (2015). Being a relatively nearby Local Group galaxy ($\mu_0 = 19.62$ mag; Martínez-Vázquez et al. 2015), Sculptor has been extensively studied as a probe for galaxy evolution, and detailed studies are available of its variable star content, with photometry stretching back over two decades (for a thorough review, see Martínez-Vázquez et al. 2016a, hereafter MV16a). We specifically chose Sculptor as a test case for our Fourier metallicity relations as this dwarf galaxy has been shown to have an early history of chemical enrichment, resulting in an older stellar population (including RRL stars) with a broad range of metallicity ($\gtrsim$1 dex; see Clementini et al. 2005; Martínez-Vázquez et al. 2015, 2016b). By studying Sculptor, we show that the relations provided in this work are widely applicable to complex stellar populations, beyond RRLs in the field or GCs.

Sculptor photometry is available from the PBS database in both the *I* band (used by MV16b in their work) and the *V* band. We refer to MV16a for the exact details of the observing runs, bands observed, instruments, and telescopes used to collect the Sculptor photometry in PBS. Out of 536 known RRLs (289 RRab, 197 RRc, and 50 RRd; MV16a), MV16b derived photometric metallicities for 276 RRab and 195 RRc stars. However, only 274 of these stars (126 RRab and 148 RRc) have good-quality *V*-band light curves (according to the criteria outlined in Paper I, Section 3). For these stars, we have extracted their *V*-band Fourier parameters following the procedures described in Section 3.1. We have then estimated their photometric [Fe/H] abundances using our Fourier metallicity relations for RRab (Equation 6 from Paper I with

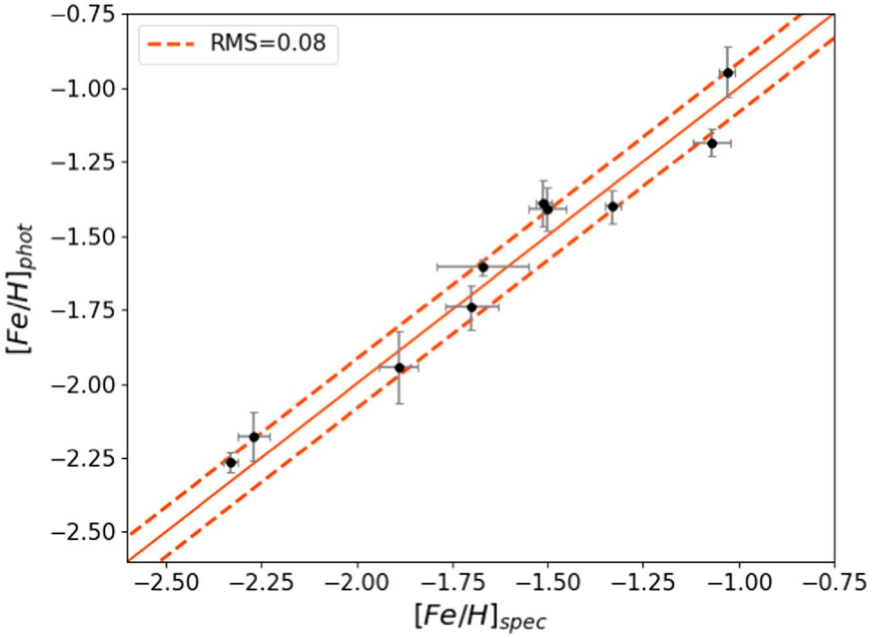

Figure 7. $[Fe/H]_{spec}$ vs. $[Fe/H]_{phot}$ obtained by using Equation (3) (this work) for RRc variables, and Equation (6) of Paper I (shifted to the scale of C09) for the RRab, in a sample of 10 GCs. The solid orange line is the 1–1 relation, and the dashed orange lines show the standard deviation (± 0.08 dex). Error bars correspond to the uncertainties in spectroscopic metallicity (from C09 and Mackey & Gilmore 2004), and the statistical error in the photometric metallicity calculated as standard deviation of the metallicity of the individual RRL in the cluster.

[Fe/H] shifted to the scale of C09) and RRc (Equation 3 from Section 3.3) stars, respectively.

The results of this analysis are shown in Figure 9. The top left panel shows the Fourier metallicity distributions of the Sculptor RRab and RRc stars. The two histograms have a similar mean (−1.88 dex and −1.83 dex for the RRab and RRc, respectively) and dispersion ($\sigma_{\rm RRab} = 0.48$ dex and $\sigma_{\rm RRc} = 0.36$ dex). The remaining panels of Figure 9 compare the metallicity distribution obtained with our Fourier method with the [Fe/H] abundance derived via PLZ inversion by MV16b. We find a remarkable agreement between the metallicities derived with these two methods. In the overall sample (RRab and RRc together, top right panel) we measured a mean metallicity [Fe/H] $\simeq -1.85$ dex, matching the value of [Fe/H] $\simeq -1.90$ dex found by MV16b. The dispersion and shape of the two [Fe/H] distributions is also very similar, with both methods suggesting a spread of metallicities in the Sculptor RRL population of ∼2 dex. Note that while the Fourier metallicities derived in this work suggest the presence of a small high-metallicity tail (with a few stars having [Fe/H] between −1.0 and −0.5 dex, which was not seen in MV16b), this excess may be an artifact originating in the calibration of our relation, as noted in Section 4.2. Comparison of the Fourier and PLZ metallicities derived for RRab and RRc separately (bottom row in Figure 9) leads to similar conclusions.

These results are also consistent with the spectroscopic metallicities of Sculptor. Clementini et al. (2005) found a [Fe/H] peaking at ∼−1.8 dex via the ΔS spectroscopic method applied to a sample of 107 RRL. Achieving such a consistent mean metallicity and distribution validates both of these photometric approaches, especially because the two photometric relations are completely independent of one another both in methodology (shape of the light curve as opposed to inversion of the PLZ relation) and in the data set used (V band versus I band, and light curves with different sampling and coverage).

5. Conclusions

In this work, we provide new relations to derive photometric metallicities based on the ϕ_{31} Fourier parameter of optical and, for the first time, infrared light curves of RRc variables. Our relations are calibrated using a large sample (approximately four times larger than anything used before at optical wavelengths) of field RRc variables for which homogeneous spectroscopic abundances are available and cover a broad range of metallicities ($-2.5 \lesssim$ [Fe/H] $\lesssim 0.0$) derived from HR spectra and the ΔS method, using techniques developed by C21. The photometric time series of our calibration stars were extracted from the ASAS-SN (V band) and the WISE (NEOWISE extension, $W1$ and $W2$ bands) surveys, providing well-sampled light curves that allow for reliable Fourier expansions.

Comparisons with other optical photometric metallicity relations for RRc variables show that our formula provides reliable [Fe/H] abundances without noticeable trends over the entire metallicity range found in the MW halo. Our V-band relation (Equation (3)) reproduces spectroscopic metallicities with a residual standard deviation of $\simeq$0.30 dex, which is smaller than the higher-order relations found in the literature. We tested our V-band relation on RRLs in GCs and showed that we can accurately estimate the average cluster metallicity with an overall accuracy of ∼0.08 dex. Additionally, we have shown that this relation can reproduce the [Fe/H] distribution of systems with a more complicated history of chemical enrichment, such as the Sculptor dSph, consistent with the predictions of both spectroscopy and other photometric relations.

For the first time, we have also obtained a mid-infrared period-ϕ_{31}-[Fe/H] relation in the WISE $W1$ and $W2$ bands (Equation (4)). Although our calibration sample is five times smaller than the V-band sample, our mid-infrared relation has a similar accuracy ($\simeq$0.29 dex) in the low- and moderate-metallicity range ([Fe/H] $\lesssim -0.5$ dex). In the high-metallicity

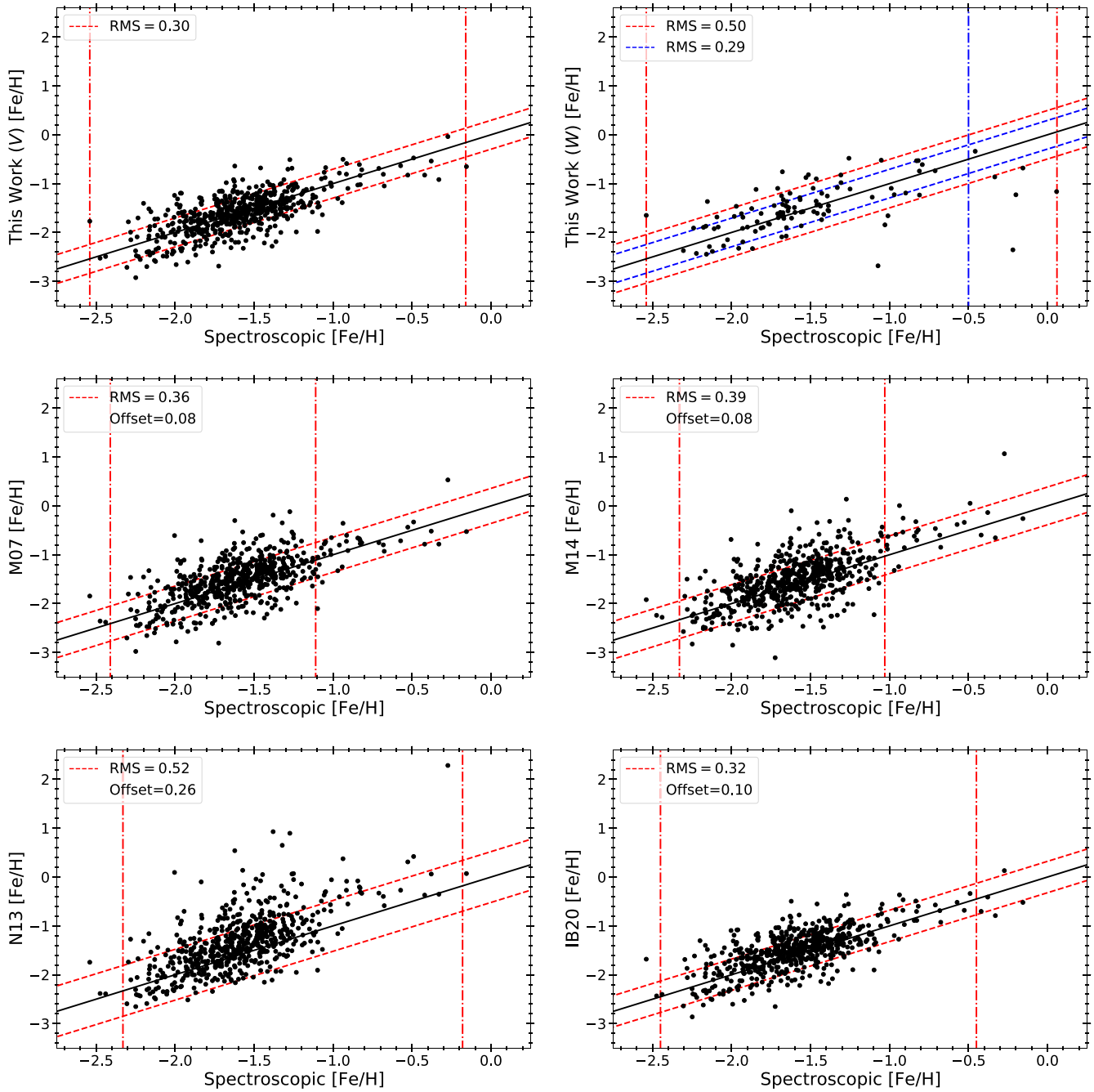

Figure 8. Comparison of the spectroscopic [Fe/H] abundances of our calibration sample and those derived with a variety of photometric metallicities, such as those presented in Section 3.1 (top row), M07 and M14 (middle row), and N13 and IB20 (bottom row). The diagonal dashed lines represent the rms dispersion about the ideal one-to-one relation. The metallicity range used to calibrate each relation is indicated by the two vertical dash–dotted red lines. An additional rms is shown for the WISE band relation (top right panel, dashed blue lines), calculated using only the stars with [Fe/H] $\lesssim -0.5$ (vertical dash–dotted blue line).

range, our relation appears to underpredict the [Fe/H] abundance expected from spectroscopy; further analysis (relying on a larger sample of solar metallicity RRc calibrators) is needed to understand the root cause of this deviation.

This work complements the analysis we presented in Paper I, where we derived similar relations for field RRab variables using the same techniques as described here (and a calibration catalog with spectroscopic metallicities derived with the same methods). Section 4.1 shows that for stellar populations where both RRab and RRc variables are found (e.g., many Galactic GCs), combining spectroscopic metallicities from RRL in both pulsation modes further improves the [Fe/H] reliability, with an accuracy of the population average metallicity approaching high-resolution spectroscopic measurements.

Whether in the mid-infrared or optical, for the RRab or RRc, the relations presented here will be crucial to facilitate the quick determination of reliable RRL metallicities for the many upcoming wide-area time-domain surveys and ELTs (such as the LSST at the Vera C. Rubin Observatory). Our mid-infrared relation will allow future telescopes (such as the JWST and the Roman telescope) to reach RRLs across the Local Group of galaxies, where spectral observations will not be feasible. Finally, by providing a method for obtaining reliable metallicities of individual RRL, Paper I and this work will be

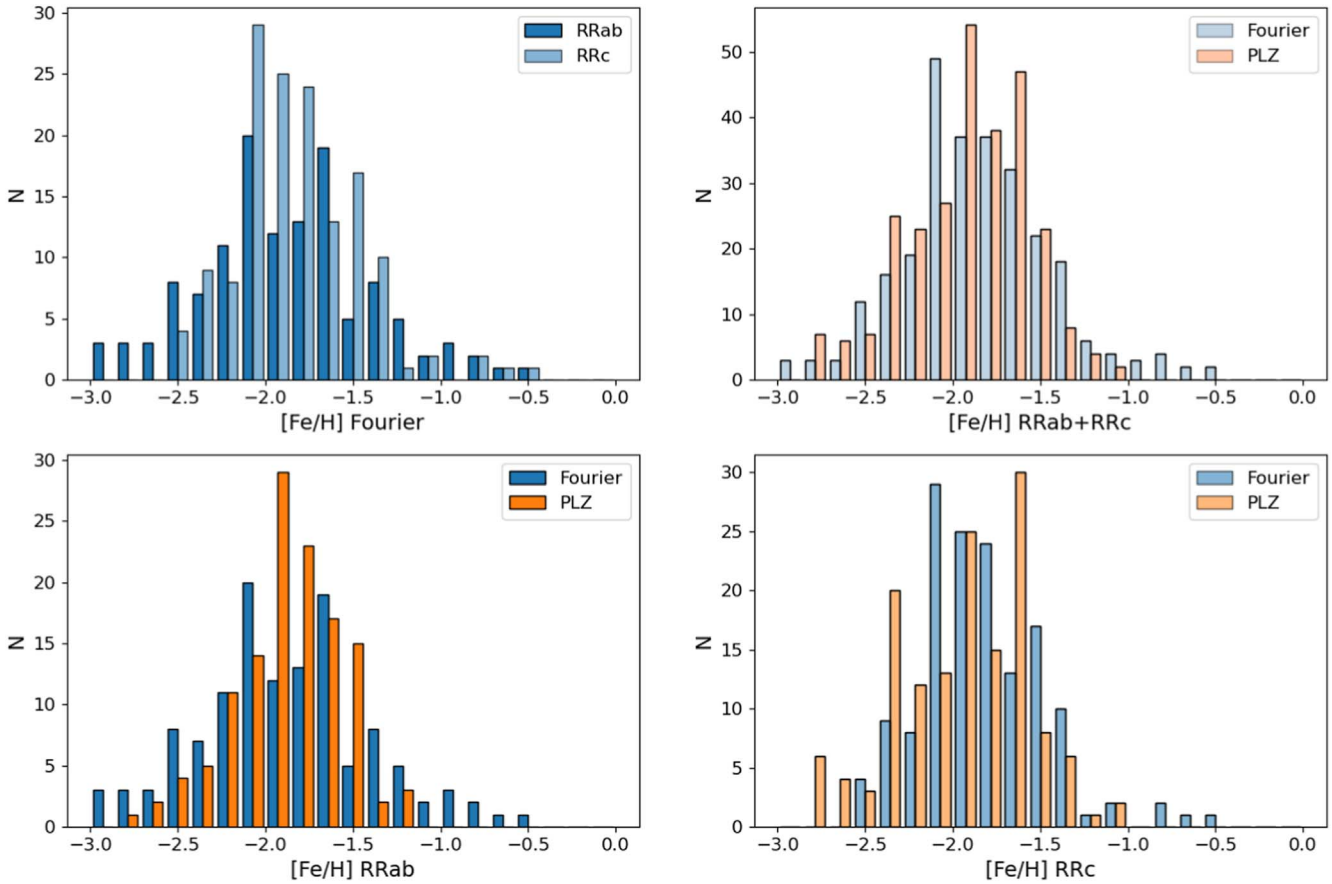

Figure 9. Comparison of derived [Fe/H] distributions of Sculptor dSph variables. *Top left*: Histogram of the [Fe/H] obtained by using the Fourier *V*-band ϕ_{31} applied to Equation (3) (this work) for RRc variables, and Equation (6) of Paper I (shifted to the scale of C09) for the RRab. The remaining panels compare the Fourier ϕ_{31} derived [Fe/H] to those derived in MV16b (through inversion of an *I*-band PLZ relation, see text) for the entire RRab+RRc sample (*top right*), and solely RRab or RRc variables (*bottom left* and *bottom right*, respectively).

crucial in determining accurate distances with PLZ and PWZ relations.

This publication makes use of data products from WISE, which is a joint project of the University of California, Los Angeles, and the Jet Propulsion Laboratory (JPL)/California Institute of Technology (Caltech), funded by the National Aeronautics and Space Administration (NASA), and from NEOWISE, which is a JPL/Caltech project funded by NASAs Planetary Science Division.

This publication also makes use of data products from the ASAS-SN project, whose telescopes are hosted by the Las Cumbres Observatory. ASAS-SN is supported by the Gordon and Betty Moore Foundation through grant GBMF5490 and the NSF by grants AST-151592 and AST-1908570. Development of ASAS-SN has been supported by the Peking University, the Mt. Cuba Astronomical Foundation, the Ohio State University Center for Cosmology and AstroParticle Physics, the Chinese Academy of Sciences South America Center for Astronomy (CASSACA), the Villum Foundation, and George Skestos.

This work has made use of data from the European Space Agency (ESA) mission Gaia (https://www.cosmos.esa.int/gaia), processed by the Gaia Data Processing and Analysis Consortium (DPAC, https://www.cosmos.esa.int/web/gaia/dpac/consortium). Funding for the DPAC has been provided by national institutions, in particular the institutions participating in the Gaia Multilateral Agreement.

Guoshoujing Telescope (the Large Sky Area Multi-Object Fiber Spectroscopic Telescope LAMOST) is a National Major Scientific Project built by the Chinese Academy of Sciences. Funding for the project has been provided by the National Development and Reform Commission. LAMOST is operated and managed by the National Astronomical Observatories, Chinese Academy of Sciences.

Funding for the SDSS and SDSS-II has been provided by the Alfred P. Sloan Foundation, the Participating Institutions, the National Science Foundation, the U.S. Department of Energy, the National Aeronautics and Space Administration, the Japanese Monbukagakusho, the Max Planck Society, and the Higher Education Funding Council for England. The SDSS Web Site is http://www.sdss.org/. The SDSS is managed by the Astrophysical Research Consortium for the Participating Institutions. The Participating Institutions are the American Museum of Natural History, Astrophysical Institute Potsdam, University of Basel, University of Cambridge, Case Western Reserve University, University of Chicago, Drexel University, Fermilab, the Institute for Advanced Study, the Japan Participation Group, Johns Hopkins University, the Joint Institute for Nuclear Astrophysics, the Kavli Institute for Particle Astrophysics and Cosmology, the Korean Scientist Group, the Chinese Academy of Sciences (LAMOST), Los Alamos National Laboratory, the Max-Planck-Institute for

Astronomy (MPIA), the Max-Planck-Institute for Astrophysics (MPA), New Mexico State University, Ohio State University, University of Pittsburgh, University of Portsmouth, Princeton University, the United States Naval Observatory, and the University of Washington.

M. Marengo and J. P. Mullen are supported by the National Science Foundation under grant No. AST-1714534.

Facilities: WISE, ASAS-SN, Gaia, LAMOST, SDSS-SEGUE.

Software: Astropy (Astropy Collaboration et al. 2013), SciPy (Virtanen et al. 2020), scikit-learn (Pedregosa et al. 2011).

ORCID iDs

Joseph P. Mullen https://orcid.org/0000-0002-1650-2764
Massimo Marengo https://orcid.org/0000-0001-9910-9230
Clara E. Martínez-Vázquez https://orcid.org/0000-0002-9144-7726
Giuseppe Bono https://orcid.org/0000-0002-4896-8841
Vittorio F. Braga https://orcid.org/0000-0001-7511-2830
Brian Chaboyer https://orcid.org/0000-0003-3096-4161
Juliana Crestani https://orcid.org/0000-0001-8926-3496
Massimo Dall'Ora https://orcid.org/0000-0001-8209-0449
Michele Fabrizio https://orcid.org/0000-0001-5829-111X
Giuliana Fiorentino https://orcid.org/0000-0003-0376-6928
Matteo Monelli https://orcid.org/0000-0001-5292-6380
Jillian R. Neeley https://orcid.org/0000-0002-8894-836X
Peter B. Stetson https://orcid.org/0000-0001-6074-6830
Frédéric Thévenin https://orcid.org/0000-0002-5032-2476

References

Abbott, T. M. C., Abdalla, F. B., Allam, S., et al. 2018, ApJS, 239, 18
Akeson, R., Armus, L., Bachelet, E., et al. 2019, arXiv:1902.05569
Astropy Collaboration, Robitaille, T. P., & Tollerud, E. J. 2013, A&A, 558, A33
Bernard, E. J., Monelli, M., Gallart, C., et al. 2009, ApJ, 699, 1742
Bernard, E. J., Monelli, M., Gallart, C., et al. 2010, ApJ, 712, 1259
Bernard, E. J., Monelli, M., Gallart, C., et al. 2013, MNRAS, 432, 3047
Bragaglia, A., Gratton, R. G., Carretta, E., et al. 2001, AJ, 122, 207
Breuval, L., Kervella, P., Wielgórski, P., et al. 2021, ApJ, 913, 38
Carretta, E., Bragaglia, A., Gratton, R., D'Orazi, V., & Lucatello, S. 2009, A&A, 508, 695
Carretta, E., & Gratton, R. G. 1997, A&AS, 121, 95
Chambers, K. C., Magnier, E. A., Metcalfe, N., et al. 2016, arXiv:1612.05560
Clementini, G., Ripepi, V., Bragaglia, A., et al. 2005, MNRAS, 363, 734
Clementini, G., Ripepi, V., Leccia, S., et al. 2016, A&A, 595, A133
Clementini, G., Ripepi, V., Molinaro, R., et al. 2019, A&A, 622, A60
Coppola, G., Marconi, M., Stetson, P. B., et al. 2015, ApJ, 814, 71
Cox, A. N., Hodson, S. W., & Clancy, S. P. 1983, ApJ, 266, 94
Crestani, J., Fabrizio, M., Braga, V. F., et al. 2021a, ApJ, 908, 20
Crestani, J., Braga, V. F., Fabrizio, M., et al. 2021b, ApJ, 914, 10
Dambis, A. K., Berdnikov, L. N., Kniazev, A. Y., et al. 2013, MNRAS, 435, 3206
Deb, S., & Singh, H. P. 2009, A&A, 507, 1729
Deng, L.-C., Newberg, H. J., Liu, C., et al. 2012, RAA, 12, 735
Drake, A. J., Djorgovski, S. G., Mahabal, A., et al. 2009, ApJ, 696, 870
Efron, B., & Tibshirani, R. 1986, StaSc, 1, 54
Fabrizio, M., Braga, V. F., Crestani, J., et al. 2021, ApJ, 919, 118
Gaia Collaboration, Brown, A. G. A., Vallenari, A., et al. 2018, A&A, 616, A1
Gardner, J. P., Mather, J. C., Clampin, M., et al. 2006, SSRv, 123, 485
Gilligan, C. K., Chaboyer, B., Marengo, M., et al. 2021, MNRAS, 503, 4719
Groenewegen, M. A. T. 2018, A&A, 619, A8
Holl, B., Audard, M., Nienartowicz, K., et al. 2018, A&A, 618, A30
Iben, I. J., & Huchra, J. 1971, A&A, 14, 293
Iorio, G., & Belokurov, V. 2020, MNRAS, 502, 5686
Ivezić, Ž., Kahn, S. M., Tyson, J. A., et al. 2019, ApJ, 873, 111
Jayasinghe, T., Kochanek, C. S., Stanek, K. Z., et al. 2018, MNRAS, 477, 3145
Jurcsik, J., & Kovacs, G. 1996, A&A, 312, 111
Koch, D. G., Borucki, W. J., Basri, G., et al. 2010, ApJL, 713, L79
Kuehn, C. A., Dame, K., Smith, H. A., et al. 2013, AJ, 145, 160
Leavitt, H. S. 1908, AnHar, 60, 87
Leavitt, H. S., & Pickering, E. C. 1912, HarCi, 173, 1
Liu, X. W., Yuan, H. B., Huo, Z. Y., et al. 2014, IAUS, 298, 310
Lomb, N. R. 1976, Ap&SS, 39, 447
Mackey, A. D., & Gilmore, G. F. 2004, MNRAS, 355, 504
Mainzer, A., Bauer, J., Grav, T., et al. 2011, ApJ, 731, 53
Marconi, M., Coppola, G., Bono, G., et al. 2015, ApJ, 808, 50
Martínez-Vázquez, C. E., Monelli, M., Bono, G., et al. 2016, CoKon, 105, 53
Martínez-Vázquez, C. E., Monelli, M., Bono, G., et al. 2015, MNRAS, 454, 1509
Martínez-Vázquez, C. E., Stetson, P. B., Monelli, M., et al. 2016a, MNRAS, 462, 4349
Martínez-Vázquez, C. E., Monelli, M., Gallart, C., et al. 2016b, MNRAS, 461, L41
Martínez-Vázquez, C. E., Monelli, M., Bernard, E. J., et al. 2017, ApJ, 850, 137
Matteucci, F. 2021, A&ARv, 29, 5
Monelli, M., Fiorentino, G., Bernard, E. J., et al. 2017, ApJ, 842, 60
Morgan, S. 2014, in IAU Symp. 301, Precision Asteroseismology, ed. J. A. Guzik et al. (Cambridge: Cambridge Univ. Press), 461
Morgan, S. M., Wahl, J. N., & Wieckhorst, R. M. 2007, MNRAS, 374, 1421
Mullen, J. P., Marengo, M., Martínez-Vázquez, C. E., et al. 2021, ApJ, 912, 144
Muraveva, T., Delgado, H. E., Clementini, G., Sarro, L. M., & Garofalo, A. 2018, MNRAS, 481, 1195
Neeley, J. R., Marengo, M., Bono, G., et al. 2015, ApJ, 808, 11
Neeley, J. R., Marengo, M., Bono, G., et al. 2017, ApJ, 841, 84
Neeley, J. R., Marengo, M., Freedman, W. L., et al. 2019, MNRAS, 490, 4254
Nemec, J. M., Cohen, J. G., Ripepi, V., et al. 2013, ApJ, 773, 181
Nemec, J. M., Smolec, R., Benkő, J. M., et al. 2011, MNRAS, 417, 1022
Ngeow, C.-C., Yu, P.-C., Bellm, E., et al. 2016, ApJS, 227, 30
Pedregosa, F., Varoquaux, G., Gramfort, A., et al. 2011, J. Mach. Learn. Res., 12, 2825, http://jmlr.org/papers/v12/pedregosa11a.html
Persson, S. E., Madore, B. F., Krzemiński, W., et al. 2004, AJ, 128, 2239
Petersen, J. O. 1986, A&A, 170, 59
Piersimoni, A. M., Bono, G., & Ripepi, V. 2002, AJ, 124, 1528
Preston, G. W. 1959, ApJ, 130, 507
Ricker, G. R., Winn, J. N., Vanderspek, R., et al. 2015, JATIS, 1, 014003
Rood, R. T. 1973, ApJ, 184, 815
Savino, A., Koch, A., Prudil, Z., Kunder, A., & Smolec, R. 2020, A&A, 641, A96
Scargle, J. D. 1982, ApJ, 263, 835
Shappee, B. J., Prieto, J. L., Grupe, D., et al. 2014, ApJ, 788, 48
Simon, N. R., & Lee, A. S. 1981, ApJ, 248, 291
Smolec, R. 2005, AcA, 55, 59
Soszyński, I., Udalski, A., Szymański, M. K., et al. 2014, AcA, 64, 177
Virtanen, P., Gommers, R., Oliphant, T. E., et al. 2020, NatMe, 17, 261
Walker, A. R. 1989, PASP, 101, 570
Wright, E. L., Eisenhardt, P. R. M., Mainzer, A. K., et al. 2010, AJ, 140, 1868
Yanny, B., Rockosi, C., Newberg, H. J., et al. 2009, AJ, 137, 4377
Zinn, R., & West, M. J. 1984, ApJS, 55, 45